

# Rationally tailoring catalysts for the CO oxidation reaction by using DFT calculations

Dengxin Yan, Henrik H. Kristoffersen, Jack K. Pedersen, and Jan Rossmeisl\*

*Department of Chemistry, University of Copenhagen, Copenhagen 2100, Denmark*

E-mail: jan.rossmeisl@chem.ku.dk

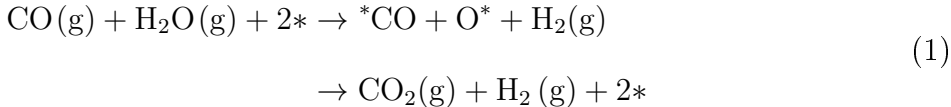
## Abstract

Rational design of catalysts by tailoring specific surface sites with different elements could result in catalysts with high activity, selectivity and stability. In this work, we show that  $\ast\text{CO}$  on-top and  $\text{O}\ast$  on-top adsorption energies are good descriptors for catalysis of the CO oxidation reaction (COOR) on pure metals and binary alloys. The observed Brønsted-Evans-Polanyi (BEP) and scaling relations for COOR on different surfaces are incorporated into a predictive model that uses the binding strength of the four adjacent metal atoms making up the active site for COOR catalysis to estimate reaction and activation energies. The model is used to screen 234 multi-metallic catalyst candidates made by combining Ru, Pt, Pd, Cu and Au at these four sites. The screening and subsequent calculations suggest that Ru-Cu-Au and Ru-Pt-Cu alloys are good catalysts for COOR. Our study shows that it is possible to use information from pure metals and binary alloys to predict the catalytic behavior of more complex alloys, and hereby reduce the computational cost of identifying new catalyst candidates for COOR.

# Introduction

Rational catalyst design is desired to accelerate the discovery of optimal catalysts for a given chemical reaction instead of relying on extensive trial-and-error experiments.<sup>1</sup> One way to achieve rational catalyst design is with the descriptor based method.<sup>2-5</sup> This method uses the often observed linear relationships between the adsorption energy of different reaction intermediates (scaling relations) and linear relationships between reaction energies and activation energies (BEP relations) to estimate the complete energy landscape of catalytic reactions on different surfaces. Once the BEP and scaling relations have been established, the catalytic behavior of new surfaces can be predicted from the adsorption energies of a few key intermediates (descriptors) on those surfaces.<sup>6</sup> The descriptor based method has been widely used for several reactions, including ammonia syntheses,<sup>7,8</sup> C–H bond breaking,<sup>9</sup> N<sub>2</sub> dissociation,<sup>10</sup> NO oxidation,<sup>11,12</sup> CO dissociation<sup>13</sup> and CO oxidation,<sup>14,15</sup> to name a few.

The COOR has been regarded as one of the most important processes in chemistry.<sup>16,17</sup> COOR is both a simple catalytic model reaction used to understand fundamental mechanisms and a key reaction step in essential chemical process such as water-gas shift, reverse water-gas shift, and methanol oxidation. We study the COOR as part of the water-gas shift reaction (eq 1), and focus on the  $\ast\text{CO} + \text{O}\ast \rightarrow \text{CO}_2(\text{g})$  step.



Previous studies of metal based catalysts, such as low index pure metal surfaces,<sup>18</sup> bimetallic alloys (PdAu,<sup>19,20</sup> PtRu,<sup>21,22</sup> PdRu,<sup>23,24</sup> PtSn,<sup>25</sup> PtCu,<sup>26</sup> AuPt<sup>27</sup>) and transition metal oxides,<sup>28</sup> have investigated COOR both experimentally and with density functional theory (DFT) calculations.

The descriptor based method for COOR requires cheap descriptors that accurately describe the adsorbate behavior on both pure metals and alloys. On pure metal surfaces, two

adsorption energies are needed for each surface, namely one for O adsorption and one for CO adsorption.<sup>29</sup> On alloy surfaces, more descriptors are likely needed because of the increased complexity. For instance, a fcc(111) surface with 5 different elements has 35 possible combinations for the three-atom hollow sites and calculating all of these is quite expensive.<sup>30</sup> If scaling relations exist for complex alloys, the extensive calculations could be avoided by using the few on-top adsorption energies to estimate the adsorption energies of the numerous hollow and bridge sites.

Transition states (TS) are usually more difficult to obtain than stable adsorption sites. It is therefore unlikely that one can find the most optimal TS for the  $\ast\text{CO} + \text{O}^\ast \rightarrow \text{CO}_2(\text{g})$  reaction on complex alloy surfaces without at least some prior knowledge or guidance. Obtaining the TS for COOR on fcc(111) surfaces is further complicated by the existence of two distinct kinds of TS, namely one between  $\ast\text{CO}$  adsorbed on-top and  $\text{O}^\ast$  adsorbed in bridge, and one between  $\ast\text{CO}$  adsorbed on-top and  $\text{O}^\ast$  adsorbed on-top. The descriptor based method can be used for guidance, if the two kinds of TS can be described by the  $\ast\text{CO}$  on-top and  $\text{O}^\ast$  on-top adsorption energies through BEP relations.

In this study, we use DFT calculations to show that  $\text{O}^\ast$  on-top and  $\ast\text{CO}$  on-top adsorption energies can be used as descriptors to estimate  $\text{O}^\ast$  bridge and  $\text{O}^\ast$  hollow adsorption energies, and the energy of the COOR TS. From these estimates, we develop a model that predicts the preferred  $\text{O}^\ast$  adsorption site (hollow, bridge or on-top), the preferred TS pathway ( $\ast\text{CO}$ -top and  $\text{O}^\ast$ -bridge or  $\ast\text{CO}$ -top and  $\text{O}^\ast$ -top) and the COOR reaction and activation energies. Finally, we construct new COOR catalyst candidates by combining Ru, Pt, Pd, Cu and Au at the four metal atom sites directly involved in COOR. The predicted reaction and activation energies are used to assess the catalytic properties of these candidates and the most interesting candidates are further examined by DFT calculations. The DFT calculations indicate that Ru-Cu-Au and Ru-Pt-Cu alloys are good catalysts for COOR.

Our study outlines a strategy that uses adsorption energies from pure metals and binary alloys to gain insight into multi-metallic surfaces. This could greatly advance the design

of new catalysts for COOR, and more generally be an approach to study highly complex catalytic systems such as high entropy alloys, which have gained a lot of attention recently.<sup>30-34</sup>

## Methods

### Computational details

The fcc(111) surfaces are modeled as slabs with  $p(4 \times 4)$  surface cells and four atomic layer thicknesses for pure metals (Au, Pd, Pt, Cu and Ru) and three atomic layer thicknesses for binary and ternary alloys ( $\text{Ag}_{11}\text{Cu}_1$ ,  $\text{Au}_3\text{Ru}$ ,  $\text{Au}_5\text{Ru}_3$ ,  $\text{AuRu}_3$ ,  $\text{Pd}_3\text{Ru}$ ,  $\text{Pt}_3\text{Ru}$ ,  $\text{Pt}_3\text{Ru}_5$ ,  $\text{Pt}_5\text{Ru}_3$ ,  $\text{Pt}_7\text{Ru}$ ,  $\text{PtCu}$ ,  $\text{PtRu}$ ,  $\text{PtRu}_3$ ,  $\text{PtRu}_7$ ,  $\text{Ru}_2\text{CuAu}$ ,  $\text{Ru}_2\text{PtAu}$ ,  $\text{Ru}_2\text{PtCu}$ ,  $\text{Au}_2\text{RuCu}$  and  $\text{RuPt}_2\text{Cu}$ ). Ru fcc is considered instead of the more stable Ru hcp. PtRu is modeled as a Pt overlayer on Ru(111)<sup>15,35</sup> and PtCu is modeled as a Cu overlayer on Pt(111) because of surface segregation.<sup>36,37</sup> The distances between periodic images of the slabs in the z direction are 16 Å. For all surfaces, the top two atomic layers are allowed to relax during geometry optimization, while the remaining metal atoms are fixed in the bulk fcc positions.

The DFT calculations are performed at the generalized gradient approximation (GGA) level with the Grid-based Projected Augmented Wave (GPAW) code<sup>38,39</sup> using the Atomic Simulation Environment (ASE) package.<sup>39</sup> The RPBE exchange correlation functional is used<sup>40</sup> and the wave functions are expanded in plane-waves with an energy cutoff of 340 eV. Due to the relative low energy cutoff, the DFT energies have some dependency on the shape of the computational box. To counter this effect, we calculate the gas phase molecules with the same box dimensions as each of the surfaces that we studied. Details are shown in Table S1 of the Supporting Information (SI).

The metal slabs are modeled with  $2 \times 2 \times 1$  k-points, while gas phase molecules are modeled with the  $\Gamma$ -point. All the surfaces are relaxed to a force below 0.1 eV/Å while gas phase molecules are relaxed below 0.01 eV/Å. The effects of zero-point energies and entropic contributions are neglected in this work. The lattice parameters for the binary and ternary

alloys are approximated by the weighted average of the DFT calculated lattice parameters of the pure metals.<sup>34</sup>

The oxygen atom tends to adsorb in the hollow sites, so constraints are needed to obtain adsorption energies for O\* on-top and O\* at bridge sites. For on-top adsorption, the O atom is initially placed directly above the metal atom and constrained to move only perpendicularly to the slab when its position is optimized. Bridge sites are considered along the x direction and the O atom is constrained to move only in the x direction and the direction perpendicularly to the slab. We do not constrain the O atom when considering hollow sites. The O\* hollow calculations can therefore relax into on-top and bridge configurations when this is preferred, resulting in the O\* hollow calculations always being more stable than the constrained on-top and bridge calculations at the same metal atoms (Figure S1 in the SI). For binary alloys with several different fcc hollow sites, the most stable fcc hollow site calculation is used in the scaling relation.

The energies of the TS ( $E_{\text{TS}}^{\text{Cal}}$ ) are calculated with the nudged elastic band (NEB) method.<sup>41</sup> The calculated COOR reaction barriers (starting from O\* in the hollow site and \*CO at the on-top site) for Pd(111) (0.97 eV) and Pt(111) (0.91 eV) are similar to previously reported values (Pd(111), 0.91 eV and Pt(111), 0.79 eV).<sup>42</sup>

The adsorption energies and relaxed structures mentioned in this work are stored in a database, which can be found online at

<http://nano.ku.dk/english/research/theoretical-electrocatalysis/>.

## COOR energy landscape

The energy landscape of the water-gas shift reaction (eq 1) is illustrated in Figure 1a. The overall reaction has a DFT reaction energy of  $-0.81$  eV compared to the experimental  $\Delta H^0(300 \text{ K})$  of  $-0.43$  eV.<sup>43</sup> Our focus is the  $\text{*CO} + \text{O*} \rightarrow \text{CO}_2(\text{g})$  reaction step, and we use the reaction energy ( $\Delta E$ ) and activation energy ( $E_a$ ) of this step to evaluate the catalytic properties of the different surfaces.  $\Delta E$  is defined in eq 2, where  $E_{\text{*CO+O*}}$  is the

energy of the  $^*\text{CO}$  and  $\text{O}^*$  co-adsorbed initial state (IS) and  $(E_{\text{CO}_2(\text{g})} + 2^*)$  is the energy of the clean surface and  $\text{CO}_2(\text{g})$ .

$$\Delta E = (E_{\text{CO}_2(\text{g})} + 2^*) - E_{^*\text{CO}+\text{O}^*} \quad (2)$$

The IS with  $\text{O}^*$  in the hollow site and  $^*\text{CO}$  at the adjacent top site is illustrated in Figure 1b. However, depending on which elements are situated at the A, B, and C surface positions,  $\text{O}^*$  may prefer to adsorb on-top or at a bridge site instead. The  $^*\text{CO}$  molecule prefers to adsorb on-top on all the pure metals except for  $\text{Pd}(111)$  (when calculated with RPBE).<sup>44</sup> For simplicity, we therefore place  $^*\text{CO}$  on top of atom D no matter what element is situated at the D position.

Finally, the activation energy ( $E_{\text{TS}}$ ) of the backward reaction step ( $\text{CO}_2(\text{g}) \rightarrow ^*\text{CO} + \text{O}^*$ ) is important, because we choose to write  $E_a$  in terms of  $E_{\text{TS}}$  and  $\Delta E$  (eq 3). This separates the difficulty of calculating the TS to  $E_{\text{TS}}$  and the difficulty of calculating the most stable  $\text{O}^*$  adsorption site to  $\Delta E$ .

$$E_a = E_{\text{TS}} + \Delta E \quad (3)$$

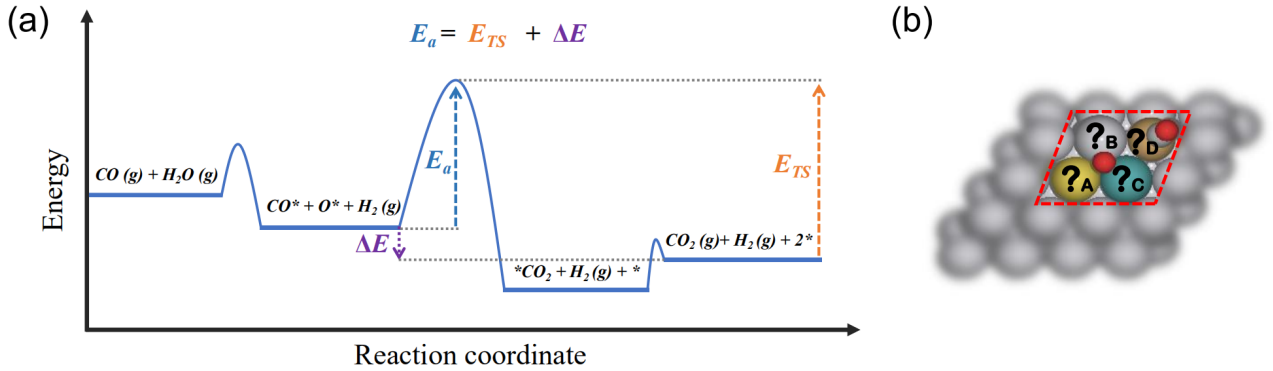


Figure 1: (a) Energy diagram for the water-gas shift reaction on surfaces.  $E_{\text{TS}}$  is the energy of the TS compared to the energy of the products ( $\text{CO}_2(\text{g})$  and  $\text{H}_2(\text{g})$ ).  $E_a$  is the activation energy and  $\Delta E$  is the reaction energy of the  $^*\text{CO} + \text{O}^* \rightarrow \text{CO}_2(\text{g})$  reaction step. (b) Illustration of the four adjacent metal atoms directly involved in COOR. The  $\text{O}^*$  atom can bind to atoms A, B and/or C, while  $^*\text{CO}$  adsorbs at atom D. We will combine Ru, Pt, Pd, Cu and Au at the A, B, C, and D to construct new catalyst candidates.

The adsorption energies of the intermediates O\* ( $\Delta E_{O^*}$ ) and \*CO ( $\Delta E_{*CO}$ ) on the surfaces are calculated using gas-phase CO, H<sub>2</sub> and H<sub>2</sub>O as references:

$$\Delta E_{O^*} = E_{O^*} - E_* - E_{H_2O(g)} + E_{H_2(g)} \quad (4)$$

$$\Delta E_{*CO} = E_{*CO} - E_* - E_{CO(g)} \quad (5)$$

$E_{O^*}$  and  $E_{*CO}$  are the DFT energies of the O\* and \*CO intermediates separately adsorbed on the surfaces.  $E_{CO(g)}$ ,  $E_{H_2O(g)}$  and  $E_{H_2(g)}$  are the DFT energies of the gas phase molecules and  $E_*$  is the DFT energy of the surfaces without any adsorbates.

## Predictive model

We build a predictive model to estimate reaction energies and activation energies for pure metals, binary alloys and multi-metallic surfaces. The model is generated in the following way. First, the adsorption energies of O\* in hollow and bridge sites are predicted using the corresponding average O\* on-top adsorption energies as descriptors (eq 6 and eq 7).

$$\Delta E_{O^*_{\text{hollow}}}^{\text{Pred}} = a \cdot \frac{1}{3} (\Delta E_{O^*_{\text{topA}}} + \Delta E_{O^*_{\text{topB}}} + \Delta E_{O^*_{\text{topC}}}) + b \quad (6)$$

$$\Delta E_{O^*_{\text{bridge}}}^{\text{Pred}} = c \cdot \frac{1}{2} (\Delta E_{O^*_{\text{topA}}} + \Delta E_{O^*_{\text{topC}}}) + d \quad (7)$$

The a, b, c and d are fitting parameters, but we choose to set a and c equal to 1.  $\Delta E_{O^*_{\text{hollow}}}^{\text{Pred}}$  and  $\Delta E_{O^*_{\text{bridge}}}^{\text{Pred}}$  are the predicted adsorption energies for O\* at hollow and bridge sites, respectively.  $\Delta E_{O^*_{\text{topA}}}$ ,  $\Delta E_{O^*_{\text{topB}}}$  and  $\Delta E_{O^*_{\text{topC}}}$  are the adsorption energies of O\* on the three adjacent top sites. To predict reaction energies ( $\Delta E^{\text{Pred}}$ ), the most stable O\* adsorption energy ( $\Delta E_{O^*_{\text{min}}}^{\text{Pred}}$ ) of top, bridge and hollow sites are used. They are calculated from eq 8 and eq 9.

$$\Delta E_{O^*_{\text{min}}}^{\text{Pred}} = \min(\Delta E_{O^*_{\text{top}}}, \Delta E_{O^*_{\text{bridge}}}^{\text{Pred}}, \Delta E_{O^*_{\text{hollow}}}^{\text{Pred}}) \quad (8)$$

$$\Delta E^{\text{Pred}} = (\Delta E_{\text{CO}_2(\text{g})} + 2*) - (\Delta E_{\text{O}^*_{\text{min}}}^{\text{Pred}} + \Delta E^*_{\text{CO}}) \quad (9)$$

There are two kinds of TS relevant to this work. The energy of the TS with \*CO-top and O\*-bridge ( $E_{\text{TS}_{\text{bri-top}}}^{\text{Pred}}$ ) is predicted by eq 10, where the average of two O\* on-top adsorption energies is used as the descriptor for O\*-bridge. The energy of the TS with \*CO-top and O\*-top ( $E_{\text{TS}_{\text{top-top}}}^{\text{Pred}}$ ) is predicted by eq 11. The e, f, g and h are fitting parameters.  $E_{\text{TS}_{\text{min}}}^{\text{Pred}}$  is the minimum TS energy of the two possible TS pathways (eq 12).

$$E_{\text{TS}_{\text{bri-top}}}^{\text{Pred}} = e \cdot (\Delta E^*_{\text{CO}_{\text{top}}} + \frac{1}{2} (\Delta E_{\text{O}^*_{\text{topB}}} + \Delta E_{\text{O}^*_{\text{topC}}})) + f \quad (10)$$

$$E_{\text{TS}_{\text{top-top}}}^{\text{Pred}} = g \cdot (\Delta E^*_{\text{CO}_{\text{top}}} + \Delta E_{\text{O}^*_{\text{topC}}}) + h \quad (11)$$

$$E_{\text{TS}_{\text{min}}}^{\text{Pred}} = \min(E_{\text{TS}_{\text{bri-top}}}^{\text{Pred}}, E_{\text{TS}_{\text{top-top}}}^{\text{Pred}}) \quad (12)$$

The predicted activation energy ( $E_a^{\text{Pred}}$ ) is finally generated as the sum of the predicted minimum TS energy and predicted reaction energy.

$$E_a^{\text{Pred}} = E_{\text{TS}_{\text{min}}}^{\text{Pred}} + \Delta E^{\text{Pred}} \quad (13)$$

Once the fitting parameters in the model have been determined, the model can in principle predict COOR reaction and activation energies on new surfaces from O\* on-top and \*CO on-top adsorption energies on those surfaces. In the last section of this paper, we go one step further and approximate the O\* on-top and \*CO on-top adsorption energies by the adsorption energies on the pure metals. This allows us to use the model on multi-metallic surfaces without first studying these surfaces with DFT. Instead, the multi-metallic surface candidates, predicted by the model to be most interesting, are further analyzed with DFT to assess how good the model is and whether the candidates remain interesting for COOR catalysis.



# Results and discussion

## Scaling relations and descriptor identification

We start by investigating the scaling relation between  $O^*$  adsorbed at fcc hollow sites and  $O^*$  adsorbed at on-top sites for several pure metals and binary alloys (Figure 2). The hollow site is situated between three metal atoms (A-B-C), we therefore use the average  $O^*$  on-top adsorption energy ( $\frac{1}{3}(\Delta E_{O^*_{\text{topA}}} + \Delta E_{O^*_{\text{topB}}} + \Delta E_{O^*_{\text{topC}}})$ ) on these three metal atoms (A, B, C) as the descriptor to estimate the  $O^*$  hollow adsorption energy. The plot shows a linear relation that is largely valid for both pure metals (where  $\Delta E_{O^*_{\text{topA}}}$ ,  $\Delta E_{O^*_{\text{topB}}}$ , and  $\Delta E_{O^*_{\text{topC}}}$  are the same) and binary alloys (where at least one of  $\Delta E_{O^*_{\text{topA}}}$ ,  $\Delta E_{O^*_{\text{topB}}}$ , and  $\Delta E_{O^*_{\text{topC}}}$  is different). The unfixed slope of the linear regression line is 0.87 (Figure S2 in the SI), however, the 95 % confidence interval for the slope is between 0.69 and 1.06, so we choose to set it to 1 to keep the model as simple as possible. A slope of 1 effectively means that the energy difference between  $O^*$  hollow and the average  $O^*$  on-top adsorption energy is constant on all surfaces. The energy difference (given by the intercept) is then  $-1.28$  eV, emphasizing the general strong preference for  $O^*$  hollow adsorption over  $O^*$  on-top adsorption.

The average on-top adsorption energy is probably the most simple choice of descriptor that could work for binary alloys. However, it is not immediately obvious that strong binding metal atoms and weak binding metal atoms should weigh equally in the hollow adsorption energy. Indeed, one of the outliers from the scaling relation is  $Au_3Ru$ , where two weak binding Au atoms and one strong binding Ru atom make up the hollow site. Fortunately, the error in  $Au_3Ru$  turns out to not be a big issue, because the Ru on-top adsorption energy is more stable than  $\Delta E_{O^*_{\text{hollowAu-Au-Ru}}}^{\text{Pred}}$ . The model will therefore use the more accurate on-top adsorption energy instead of the poorly predicted hollow adsorption energy for  $Au_3Ru$  (the same is true for  $Pd_3Ru$ ).

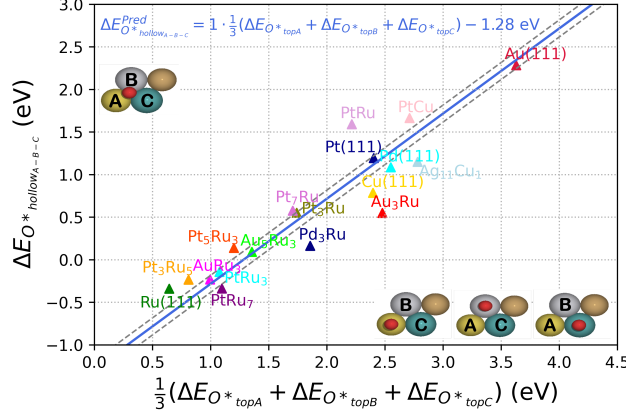


Figure 2: Linear scaling relation between the average adsorption energy of O\* on three adjacent top sites ( $\frac{1}{3}(\Delta E_{O^*_{\text{topA}}} + \Delta E_{O^*_{\text{topB}}} + \Delta E_{O^*_{\text{topC}}})$ ) versus the adsorption energy of O\* at the three-fold hollow site ( $\Delta E_{O^*_{\text{hollowA-B-C}}}$ ). The plot includes pure metals (Au, Cu, Pd, Pt and Ru) and binary alloys (Ag<sub>11</sub>Cu<sub>1</sub>, Au<sub>3</sub>Ru, Au<sub>5</sub>Ru<sub>3</sub>, AuRu<sub>3</sub>, Pd<sub>3</sub>Ru, Pt<sub>3</sub>Ru, Pt<sub>3</sub>Ru<sub>5</sub>, Pt<sub>5</sub>Ru<sub>3</sub>, Pt<sub>7</sub>Ru, PtCu, PtRu, PtRu<sub>3</sub> and PtRu<sub>7</sub>). The dashed lines are  $\pm 0.1$  eV offset from the blue line. The adsorption energies used in the plot are tabulated in Table S2 in the SI.

Another linear scaling relation exists between the average O\* on-top adsorption energy ( $\frac{1}{2}(\Delta E_{O^*_{\text{topA}}} + \Delta E_{O^*_{\text{topC}}})$ ) on two neighboring top sites (A and C) and the O\* adsorption energy ( $\Delta E_{O^*_{\text{bridge}}}$ ) at the bridge site (A-C) (Figure 3). The slope of the free linear regression line is 0.84 with the 95 % confidence interval between 0.64 and 1.04 (Figure S3 in the SI). The scaling relations for O\* bridge and O\* hollow adsorption have very similar slopes and this indicates that their energy difference is on average constant across different metal surfaces. We again set the slope to 1 and obtain an intercept of  $-0.48$  eV making O\* bridge adsorption on average 0.8 eV less stable than O\* hollow adsorption (obtained from the difference in intercepts). If we assume that the O\* bridge adsorption sites are good representations for the TS of O\* diffusion on fcc(111) surfaces, our scaling relations indicate that O\* diffusion has a constant activation energy of 0.8 eV on pure metal surfaces. A study<sup>45</sup> have found that the O\* diffusion barriers on pure metal fcc(111) surfaces are indeed relative constant but smaller than our result (between 0.33 eV and 0.59 eV). The constant energy differences between O\* adsorption at hollow, bridge, and on-top sites are only strictly present on pure metal surfaces, because the adsorption energies are connected by *average* O\* on-top adsorption

energies. The constant energy differences are broken on alloy surfaces and we will explore this in the next section.

In Figure 3, the  $\text{Au}_3\text{Ru}$  and  $\text{Pd}_3\text{Ru}$  surfaces again deviate from the optimum scaling line, because the  $\text{O}^*$  bridge adsorption ends up looking every much like  $\text{O}^*$  on-top adsorption on the Ru atom. Still, the scaling relation demonstrates that it is possible to use average  $\text{O}^*$  on-top adsorption energies as descriptors instead of calculating  $\text{O}^*$  bridge adsorption energies.

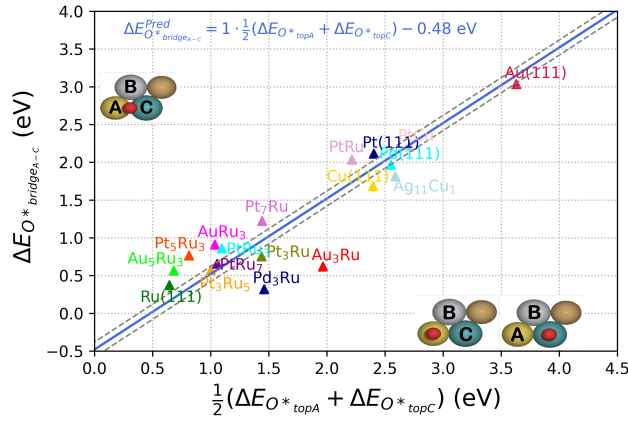


Figure 3: Linear scaling relation between the average  $\text{O}^*$  on-top adsorption energy for two neighboring sites ( $\frac{1}{2}(\Delta E_{\text{O}^*_{\text{topA}}} + \Delta E_{\text{O}^*_{\text{topC}}})$ ) versus the adsorption energy of  $\text{O}^*$  on the bridge site between the two top sites ( $\Delta E_{\text{O}^*_{\text{bridgeA-C}}}$ ). The plot includes pure metals (Au, Cu, Pd, Pt and Ru) and binary alloys ( $\text{Ag}_{11}\text{Cu}_1$ ,  $\text{Au}_3\text{Ru}$ ,  $\text{Au}_5\text{Ru}_3$ ,  $\text{AuRu}_3$ ,  $\text{Pd}_3\text{Ru}$ ,  $\text{Pt}_3\text{Ru}$ ,  $\text{Pt}_3\text{Ru}_5$ ,  $\text{Pt}_5\text{Ru}_3$ ,  $\text{Pt}_7\text{Ru}$ ,  $\text{PtCu}$ ,  $\text{PtRu}$ ,  $\text{PtRu}_3$  and  $\text{PtRu}_7$ ). The dashed lines are  $\pm 0.1$  eV offset from the blue line. The adsorption energies used in the plot are tabulated in Table S3 in the SI.

The  $\text{O}^*$  on-top adsorption energies are simple descriptors, from which the more convoluted  $\text{O}^*$  adsorption energies at hollow and bridge sites can be estimated even when these sites are made up of two different elements. Intuitively, it is more difficult to construct an inverse scaling relation, where single metal on-top adsorption energies are estimated from multi-element  $\text{O}^*$  bridge or  $\text{O}^*$  hollow adsorption energies, and we have not pursued that possibility.

## Preferred oxygen adsorption sites

The scaling relations connect the  $\Delta E_{\text{O}^*_{\text{top}}}$ ,  $\Delta E_{\text{O}^*_{\text{bridge}}}$  and  $\Delta E_{\text{O}^*_{\text{hollow}}}$  adsorption energies. The relations can therefore be used to identify which of these sites is the most stable O\* adsorption site. Two boundary lines are constructed by setting  $\Delta E_{\text{O}^*_{\text{hollow}}}^{\text{Pred}} = \Delta E_{\text{O}^*_{\text{topC}}}$  (eq 14) and  $\Delta E_{\text{O}^*_{\text{hollow}}}^{\text{Pred}} = \Delta E_{\text{O}^*_{\text{bridge}}}^{\text{Pred}}$  (eq 15).

$$\Delta E_{\text{O}^*_{\text{hollow}}}^{\text{Pred}} = \frac{1}{3} (\Delta E_{\text{O}^*_{\text{topA}}} + \Delta E_{\text{O}^*_{\text{topB}}} + \Delta E_{\text{O}^*_{\text{topC}}}) - 1.28 \text{ eV} = \Delta E_{\text{O}^*_{\text{topC}}} \quad (14)$$

$$\begin{aligned} \Delta E_{\text{O}^*_{\text{hollow}}}^{\text{Pred}} &= \Delta E_{\text{O}^*_{\text{bridge}}}^{\text{Pred}} \\ \frac{1}{3} (\Delta E_{\text{O}^*_{\text{topA}}} + \Delta E_{\text{O}^*_{\text{topB}}} + \Delta E_{\text{O}^*_{\text{topC}}}) - 1.28 \text{ eV} &= \frac{1}{2} (\Delta E_{\text{O}^*_{\text{topA}}} + \Delta E_{\text{O}^*_{\text{topC}}}) - 0.48 \text{ eV} \end{aligned} \quad (15)$$

These lines separate the region where bridge adsorption is preferred and the region where top adsorption is preferred from where hollow adsorption is preferred, as a function of  $\Delta E_{\text{O}^*_{\text{topA}}}$ ,  $\Delta E_{\text{O}^*_{\text{topB}}}$ , and  $\Delta E_{\text{O}^*_{\text{topC}}}$ .

The preferred O\* adsorption sites (top, bridge or hollow) are plotted in Figure 4. Two cases are worth considering; the first is when the C atom is the strongest binding atom ( $\Delta E_{\text{O}^*_{\text{topC}}} \leq \Delta E_{\text{O}^*_{\text{topA}}}, \Delta E_{\text{O}^*_{\text{topB}}}$ ) (Figure 4a). The black dotted line is given by eq 14 and separates where O\* on-top and O\* hollow adsorption is most stable. The line shows that it is possible to favor on-top adsorption over hollow adsorption, if the O\* atom adsorbs much stronger on the C atom than on the A and B atoms combined. The plot also contains points representing O\* adsorption on the surfaces we have studied, which again shows that O\* hollow adsorption is always preferred on pure metals. However, Au<sub>3</sub>Ru and Pd<sub>3</sub>Ru are placed in the O on-top adsorption zone, because O\* adsorption on Ru is much stronger than O\* adsorption on Au and Pd.

We again note that O\* hollow adsorption is calculated without constraints, whereas O\* on-top and O\* bridge calculations are constrained to be directly on top of the metal atom or somewhere between the two metal atoms, respectively. The O\* hollow calculation relaxes into an on-top or bridge configuration when this is favorable and O\* hollow is therefore always

found to be most stable. However, the O\* hollow calculation is then not necessarily well described by the O\* hollow scaling relation (Figure 2), but is described by either the on-top adsorption energy ( $\Delta E_{\text{O}^*_{\text{topC}}}$ ) or the O\* bridge scaling relation (Figure 3). For instance, the most stable O\* hollow calculations for Au<sub>3</sub>Ru and Pd<sub>3</sub>Ru have relaxed into configurations that seem very much on-top like, and have adsorption energies that are 0.10 eV and 0.14 eV more stable than the O\* on-top adsorption energies on the Ru atoms (Figure S1, Table S2 and Table S3 in the SI). The O\* on-top adsorption energies are therefore much closer to the calculated O\* hollow adsorption energies for Au<sub>3</sub>Ru and Pd<sub>3</sub>Ru than the predicted O\* hollow adsorption energies (Figure 2).

The second interesting case is when the B atom is the weakest binding atom ( $\Delta E_{\text{O}^*_{\text{topB}}} \geq \Delta E_{\text{O}^*_{\text{topA}}}, \Delta E_{\text{O}^*_{\text{topC}}}$ ) (Figure 4b). The blue dotted line is derived from eq 15 and the points above this line prefer O\* adsorption in hollow sites compared to adsorption at bridge sites. However, if the O\* on-top adsorption energy on atom B is much weaker than the other two top energies, O\* bridge adsorption on atoms A and C is preferred. Au<sub>5</sub>Ru<sub>3</sub> lies in the bridge zone, and again the O\* hollow calculation relaxes into a bridge configuration on two Ru atoms (Figure S1 in the SI). The resulting adsorption energy is well described by both the O\* bridge and O\* hollow scaling relations.

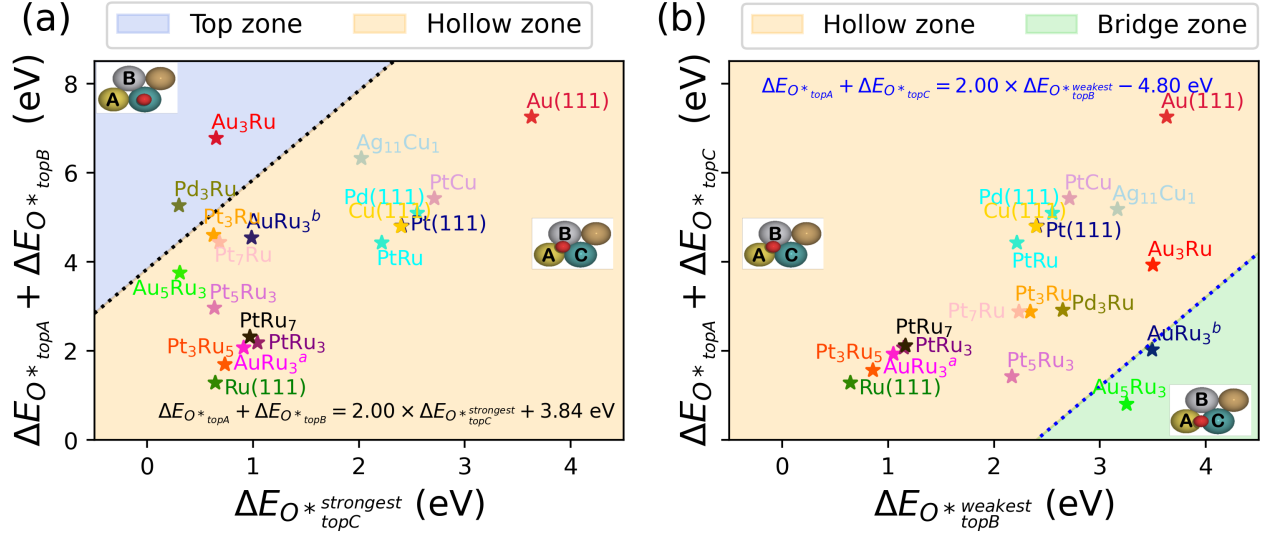


Figure 4: Preferred O\* adsorption site. (a) On-top versus hollow sites. The black dotted line is given by eq 14 and represents where on-top and hollow adsorption are equally stable.  $\Delta E_{O^*}^{\text{strongest topC}}$  is the most stable O\* adsorption energy of the three adjacent top sites. (b) Bridge versus hollow sites. The blue dotted line is given by eq 15 and represents where bridge and hollow adsorption are equally stable.  $\Delta E_{O^*}^{\text{weakest topB}}$  is the weakest O adsorption energy of the three adjacent top sites. AuRu3<sup>a</sup> is the most stable three-fold hollow site on AuRu3, while AuRu3<sup>b</sup> is a less stable (metastable) three-fold hollow site on AuRu3 (Figure S4 in the SI).

## The Brønsted-Evans-Polanyi (BEP) relations

The remaining part of the descriptor based method is to predict the COOR TS through BEP relations and avoid additional NEB calculations. On pure metals, COOR occurs via the Langmuir-Hinshelwood mechanism<sup>46</sup> and at the TS \*CO is sitting on-top and O\* is sitting at the adjacent bridge site.<sup>42,47</sup> However, on more complicated alloys the \*CO-top and O\*-top TS is preferred when the O\* on-top adsorption site is more stable than the O\* bridge site. Therefore, BEP relations for both situations have to be constructed.

A linear BEP relation for the \*CO-top and O\*-bridge TS is plotted in Figure 5a using the descriptor  $\Delta E^*_{\text{CO-top}} + \frac{1}{2} (\Delta E_{O^*}^{\text{topB}} + \Delta E_{O^*}^{\text{topC}})$ . The BEP relation includes the five pure metals (Au, Cu, Pd, Pt and Ru) and two binary alloys (PtRu and Pt3Ru). We use the backward reaction activation energy ( $E_{\text{TS}}$ ) to plot the BEP relation, since it does not

depend on the complicated O\* adsorption configuration in the O\* + \*CO IS. The slope of this BEP relation is 0.62, which is similar to previous work.<sup>48</sup> The BEP relation includes two reactions on Pt<sub>3</sub>Ru, which have similar IS and final state, but different TS with O\* sitting in a Pt-Pt bridge or a Pt-Ru bridge configuration. The two reactions also have very different E<sub>TS</sub> and this means that the descriptor has to capture the different O\* bridge configurations. The \*CO-top and O\*-bridge TS can therefore be described by  $\Delta E_{*CO_{top}} + \frac{1}{2} (\Delta E_{O*_{topB}} + \Delta E_{O*_{topC}})$  and  $\Delta E_{*CO_{top}} + \Delta E_{O*_{bridge}}$ , but not fully by  $\Delta E_{*CO_{top}} + \Delta E_{O*_{hollow}}$  (Figure S9 in the SI).

The \*CO-top and O\*-top TS has a separate BEP relation, where the E<sub>TS</sub> is a linear function of  $\Delta E_{*CO_{top}} + \Delta E_{O*_{topC}}$  (Figure 5b). The BEP relation is again plotted for five pure metals (Au, Cu, Pd, Pt and Ru) and two binary alloys (Pt<sub>3</sub>Ru and Pd<sub>3</sub>Ru). The slope of this BEP relation is 0.75 and this relation will be used in our model to describe the cases that prefer the \*CO-top and O\*-top TS.

The slopes in the two BEP relations are indicative of how much of the \*CO-top and O\*-bridge or \*CO-top and O\*-top nature is retained at the TS. Both the \*CO and O\* species are expected to adsorb with two bonds to the surface, so the 0.62 and 0.75 slopes indicate that one surface bond from each species is partly broken at the TS. This in turn makes it possible for the \*CO and O\* species to start forming a bond between them. The intercepts in the two BEP relations are 0.94 eV for \*CO-top and O\*-bridge and 1.46 for \*CO-top and O\*-top TS. The difference matches the general preference for O\*-bridge over O\*-top adsorption also observed in the O\*-bridge scaling relation (Figure 3). The \*CO-top and O\*-bridge TS is therefore preferred for all the pure metals<sup>19,42,49</sup> and most binary alloys. The \*CO-top and O\*-top TS is only preferred when the O\* on-top site is more stable than the O\* bridge site.

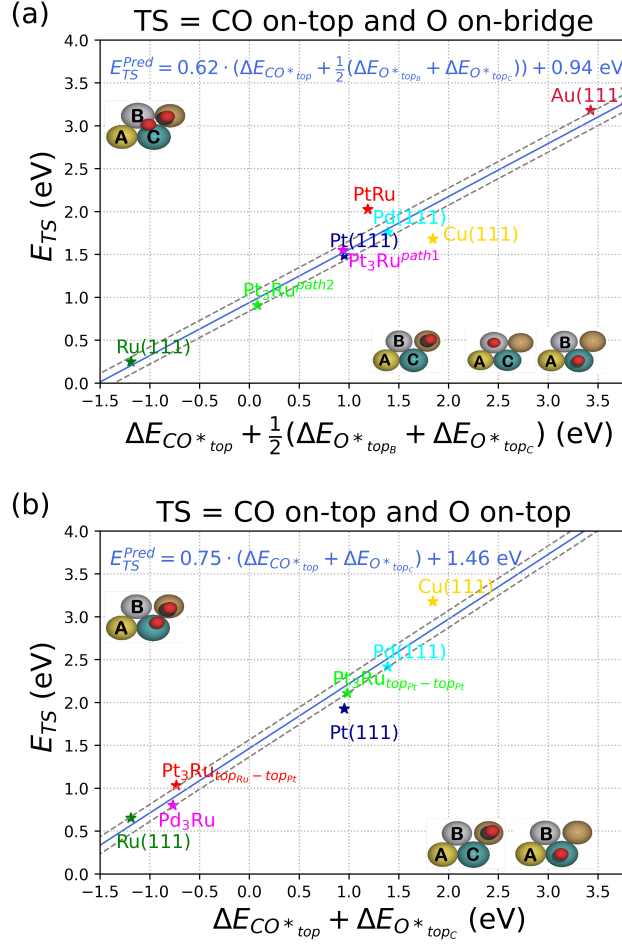


Figure 5: (a) BEP relation between the  $^*CO$ -top and  $O^*$ -bridge  $E_{TS}$  and the sum of the  $^*CO$  on-top adsorption energy and the average of two  $O^*$  on-top adsorption energies. Figure S6 and S7 in the SI show the NEB pathways going through  $^*CO$ -top and  $O^*$ -bridge TS.  $Pt_3Ru^{path1}$  and  $Pt_3Ru^{path2}$  are the different pathways with  $O^*$  going through the Pt-Pt and Pt-Ru TS, respectively. (b) BEP relation between the  $^*CO$ -top and  $O^*$ -top  $E_{TS}$  and the sum of the  $^*CO$  on-top adsorption energy and the  $O^*$  on-top adsorption energy. Figure S8 in the SI shows the NEB pathways going through  $^*CO$ -top and  $O^*$ -top TS. The dashed lines are  $\pm 0.1$  eV offset from the blue lines.

## A model for predicting $E_a$

The predictive model for the COOR activation energy ( $E_a$ ) is obtained by combining the observed scaling relations and BEP relations. Figure 6 shows a parity plot that compares the predicted values for  $E_a$  to the calculated ones. The reaction barrier for Ru(111) is overestimated by the model.  $E_{TS}$  is quite well predicted for Ru(111) (Figure S10 in the SI),



so the error in  $E_a$  must mainly come from the prediction of the  $O^* + ^*CO$  IS, and indeed the  $O^*$  hollow adsorption energy is not predicted that well on Ru(111) (Figure 2). For the pure metals and PtRu and Pt<sub>3</sub>Ru binary alloys the IS is  $O^*$  hollow and  $^*CO$  on-top, and the TS is  $O^*$  bridge and  $^*CO$  on-top. However, this is not always the case for the more complicated alloys.

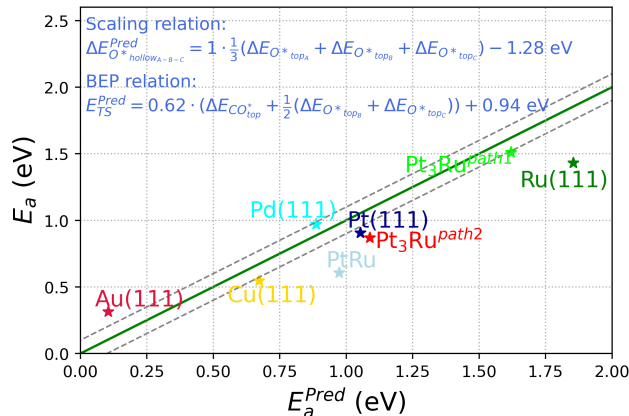


Figure 6: Parity plot that compares the predicted activation energies ( $E_a^{\text{Pred}}$ ) to the calculated ones ( $E_a$ ). The dashed lines are  $\pm 0.1$  eV offset from the green ideal prediction line.

We note that our model could be built with  $^*COOH$  on-top adsorption energies instead of  $^*CO$ , because there is a scaling relation between these two species (Figure S11 in the SI). It might be convenient to use  $^*COOH$  as the descriptor instead of  $^*CO$ , when studying other reactions that include a COOR step, such as methanol oxidation, where both  $^*CO$  and  $^*COOH$  are possible intermediates.<sup>50,51</sup> The transition state energies ( $E_{\text{TS}}$ ) would then be described by  $(\Delta E_{^*COOH} + \frac{1}{2} \cdot (\frac{1}{2}(E_{O^*topA} + E_{O^*topB})))$  and  $(\Delta E_{COOH^*} + \frac{1}{2}E_{O^*topA})$  with slopes of 1.17 and 1.50 (Figure S12 in the SI).

## Tailoring the COOR catalytic site

Our predictive model has been built using information from pure metals and binary alloys, nevertheless, we will now try and apply it to multi-metallic surfaces. Specifically, we wish to predict which combinations of elements (Au, Cu, Pd, Pt and Ru) at the four metal sites

involved in COOR (Figure 1b) are best for COOR catalysis. This requires one additional approximation, namely that we can use the pure metal O\* on-top and \*CO on-top adsorption energies instead of having to obtain on-top adsorption energies on the multi-metallic surface. The approximation hereby neglects all ligand effects from the metal atoms surrounding the adsorbing metal atoms.<sup>52</sup>

Initially, 625 candidates are made by combining Au, Cu, Pd, Pt and Ru at atoms A, B, C and D. However, CO adsorbs very weakly on Au giving a prohibitively low \*CO coverage, so candidates with Au at atom D are excluded. Additionally, Pt and Pd have high affinity for \*CO compared to Cu, so candidates with Cu at atom D are excluded when they also contain Pd or Pt. Finally, candidates that are equivalent when swapping atom B and C are only considered once. These restrictions leave 234 remaining candidates.

We identify the most stable O\* adsorption site at atoms A, B and C and the most stable TS at atoms B and C for each candidate. The candidates are plotted in Figure 7 according to their predicted reaction energy ( $\Delta E^{\text{Pred}}$ ) and predicted activation energy ( $E_a^{\text{Pred}}$ ). We highlight the complexity of COOR on fcc(111) surfaces by plotting O\* hollow, O\* bridge and O\* on-top IS with circles, triangles and diamonds, respectively, and by plotting \*CO-top and O\*-bridge TS in black and \*CO-top and O\*-top TS in magenta. It turns out that at least one candidate exists for every combination of the three IS and two TS.

The calculated  $E_a$  and  $\Delta E$  for the pure metals (Au, Cu, Pd, Pt and Ru) are also plotted in Figure 7 (red circles). The pure metals by themselves map out a BEP relation for COOR, i.e.  $E_a$  gets smaller at more negative  $\Delta E$ . However, it is clear that some of the predicted candidates lie well below the pure metal BEP relation and have low predicted activation energies without having as negative predicted reaction energies. Our model reveals one way to improve upon the pure metals, namely by changing the element at position A to something that binds O\* weaker than the metals at positions B and C. This will weaken the IS, but according to our model not affect  $E_{\text{TS}}$  hereby reducing  $E_a$ . The study<sup>53</sup> by Z. Wang and P. Hu uses a different approach than ours to rationally tailor multi-metallic surfaces for COOR

and also find that they can break the pure metal BEP relations. Their COOR active site seems to use the above strategy with strong binding Ir atoms at positions B and C and the weaker binding Pd at position A.

The catalyst candidates need to fulfill three requirements to be good catalysts for COOR. Firstly, they should have the lowest possible  $E_a$ . Secondly, the reaction energy should be less downhill than  $-0.8$  eV such that the  $^*O + ^*CO$  IS is downhill in DFT reaction energy compared to the water gas shift reactants ( $CO(g) + H_2O(g)$ ). And thirdly, the reaction energy should not be too much uphill such that  $CO_2(g)$  formation is possible and the backreaction is not overly favored. The green area in Figure 7 indicate the optimal catalyst region and is defined by having  $E_a < 0.9$  eV and reaction energy in the interval  $-0.8 < \Delta E < 0.5$  eV. The predicted points that lie somewhat close to the green area are therefore interesting for further analyzes.

We constructed ternary alloys with COOR active sites matching eight of our most interesting candidates and calculated their  $E_a$  and  $\Delta E$  with DFT (Figure S13 in the SI shows the NEB pathways for the ternary alloys). We use the notation **ABCD** for the calculations to show which elements are at the A, B, C, and D positions, respectively. The DFT values are plotted with blue circles in Figure 7 and the deviation from the predicted values are shown by gray arrows. Here, we also include the two reactions on  $Pt_3Ru$  and the single reaction on  $Pd_3Ru$  to obtain 11 data points for validating our predictive model. The TS pathway predicted to be most stable is also the one found by the DFT NEB calculation in every case except for the  $Pt$ **PtRu** $Pt$  system (i.e.  $Pt_3Ru^{path2}$ ), where both the predicted and calculated energy difference between the two kinds of TS are very small (around 0.1 eV). The full set of predicted and calculated transition state energies, reaction energies and activation energies are compared in Table 1. Interestingly, the prediction for  $E_{TS}$  is actually more accurate (root-mean-square error of 0.21 eV) than the prediction for  $\Delta E$  (root-mean-square error of 0.34 eV), which indicate that our descriptor based model has some problems describing the  $O^*$  hollow,  $O^*$  bridge and/or  $O^*$  on-top IS possibilities. Opposite to the predicted TS

energy, the predicted  $^*\text{O} + ^*\text{CO}$  IS energy can likely be improved with a limited number of DFT calculations of  $\text{O}^*$  adsorption on the multi-metallic surfaces. Still, the errors are small enough that the model provides very useful insight into COOR on multi-metallic surfaces.

The DFT calculations place the  $\text{AuRuRuCu}$ ,  $\text{AuAuRuCu}$  and  $\text{CuPtRuPt}$  candidates most optimally in the green region of Figure 7. This indicates that Ru-Cu-Au and Ru-Pt-Cu alloys are promising catalyst candidates for COOR. The Ru-Pd catalyst (based on  $\text{PdRuPdPd}$ ) is also predicted to be a good catalyst with proper reaction energy but a little bit higher activation energy. The catalytic properties of Pd-Ru have been confirmed experimentally.<sup>23,24,54</sup>

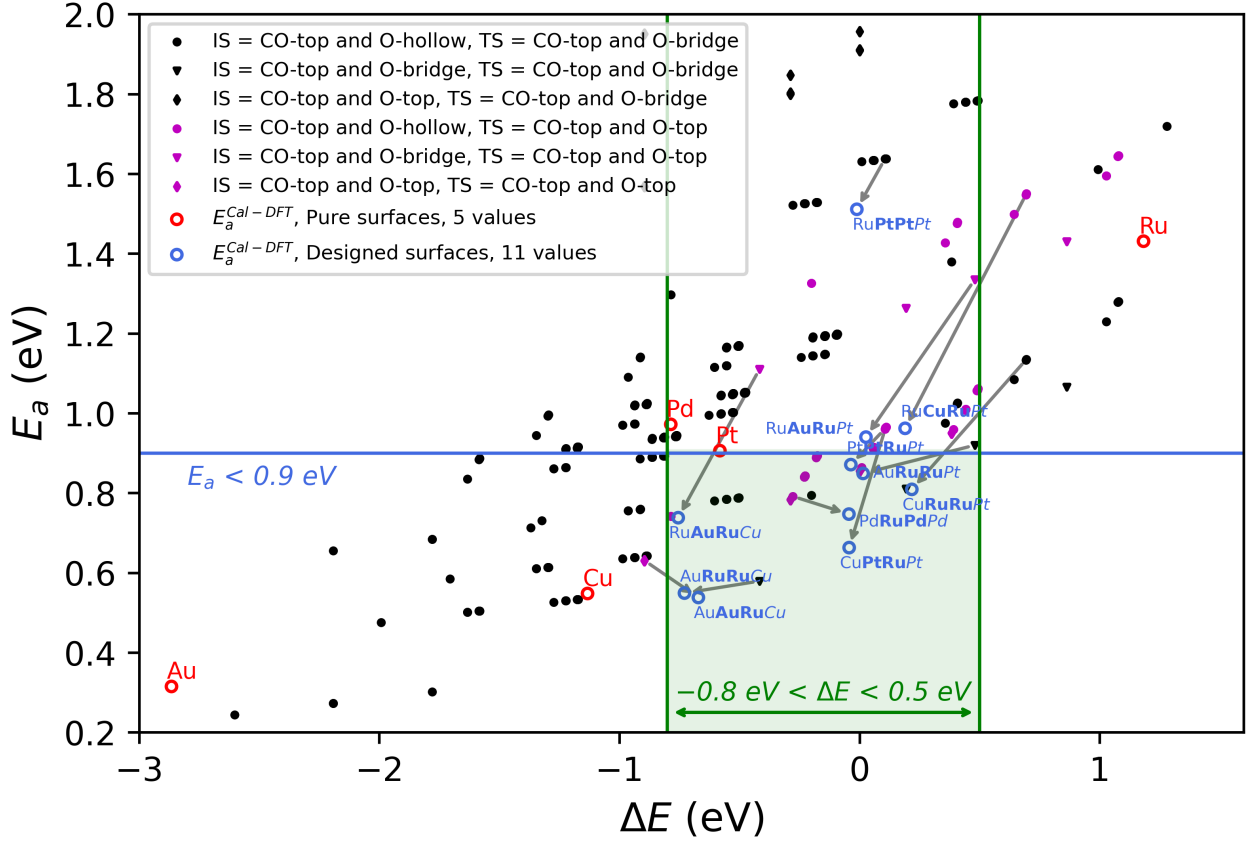


Figure 7: Reaction energies ( $\Delta E$ ) versus activation energies ( $E_a$ ) predicted for multi-metallic catalyst candidates obtained by combining Ru, Pt, Pd, Cu and Au at the four metal sites directly involved in COOR. The catalyst candidates either have O\* hollow, O\* bridge or O\* on-top IS and these are distinguished by circles, triangles and diamonds, respectively. Catalyst candidates with the \*CO-top and O\*-bridge TS are plotted in black, whereas candidates with the \*CO-top and O\*-top TS are plotted in magenta. The plot also include DFT calculated values for the pure metals (red circles) and ternary metals (blue circles). The error between predicted and DFT calculated values are shown by grey arrows. The green area is the optimal catalyst region, where the catalysts have both low activation energies and proper reaction energies.

Table 1: Predicted and DFT calculated transition state energies (eV), reaction energies (eV) and activation energies (eV) on multi-metallic surfaces for COOR.

Surfaces <sup>a</sup>	E <sub>TSmin</sub> <sup>Pred</sup>	E <sub>TS</sub>	$\Delta E^{\text{Pred}}$	$\Delta E$	E <sub>a</sub> <sup>Pred</sup>	E <sub>a</sub>
Pt <b>PtRu</b> <i>Pt</i>	0.85	0.91	0.11	-0.04	0.96	0.87
Ru <b>PtPt</b> <i>Pt</i>	1.53	1.52	0.11	-0.01	1.64	1.51
Pd <b>RuPd</b> <i>Pd</i>	1.07	0.79	-0.28	-0.04	0.79	0.75
Au <b>RuRu</b> <i>Cu</i>	1.00	1.28	-0.42	-0.73	0.58	0.55
Ru <b>AuRu</b> <i>Cu</i>	1.53	1.49	-0.42	-0.76	1.11	0.74
Au <b>RuRu</b> <i>Pt</i>	0.44	0.83	0.48	0.01	0.92	0.85
Ru <b>AuRu</b> <i>Pt</i>	0.85	0.91	0.48	0.03	1.33	0.94
Cu <b>RuRu</b> <i>Pt</i>	0.44	0.59	0.70	0.22	1.13	0.81
Ru <b>CuRu</b> <i>Pt</i>	0.85	0.77	0.70	0.19	1.55	0.96
Cu <b>RuPt</b> <i>Pt</i>	0.85	0.71	0.11	-0.04	0.96	0.66
Au <b>AuRu</b> <i>Cu</i>	1.53	1.21	-0.90	-0.67	0.63	0.54
RMSE <sup>b</sup>	0.21		0.34		0.28	

<sup>a</sup> The atoms in **bold font** are the ones that bind O\* at the TS, the atom in *italic font* is the one that binds \*CO. <sup>b</sup> RMSE is the root-mean-square error between predicted and DFT calculated values.

## Conclusions

We show that scaling relations based on O\* on-top adsorption energies can estimate the O\* bridge and O\* hollow adsorption energies and predict the most stable O\* adsorption site. On pure metal surfaces, the O\* hollow adsorption sites are always around 0.8 eV more stable than the O\* bridge sites and around 1.3 eV more stable than the O\* on-top sites. These energy differences are broken on alloy surfaces and the scaling relations capture this when the average O\* on-top adsorption energy is used as the descriptor.

We further use the O\* on-top and \*CO on-top adsorption energies in a descriptor based model to estimate the COOR transition state, reaction energy and activation energy. The model can reasonably accurately predict the feasibility of COOR on ternary alloys, even though it only has input from pure metals and binary alloys and uses the simple on-top adsorption energies as descriptors. We therefore use the model to screen new COOR catalyst candidates made by combining Au, Cu, Pd, Pt and Ru at the four adjacent metal positions making up the active site for COOR catalysis. The candidates that the model predict to

have both low activation energy and appropriate reaction energy are analyzed with DFT, which suggest that Ru-Cu-Au and Ru-Pt-Cu alloys are good catalysts for COOR.

More generally, we have outlined a strategy to use adsorption energies from pure metals and binary alloys to gain insight into multi-metallic surfaces. This could greatly advance the design of new catalysts for COOR, but also be an approach to study other highly complex catalytic systems.

## Acknowledgement

The authors acknowledge support from the Danish National Research Foundation Center for High-Entropy Alloy Catalysis (CHEAC) DNRF-149 and VILLUM FONDEN (research grant 9455). J.K.P thanks for the support from the Danish Ministry of Higher Education and Science (Structure of Materials in Real Time (SMART) grant), and D.Y. thanks for the support from the China Scholarship Council (CSC).

## Supporting Information Available

- DFT energies of gas phase molecules in different computational boxes matching the different surfaces; configurations and adsorption energies of O\* adsorbed on-top, bridge and hollow sites on binary alloys; linear scaling relations with unfixed slopes; linear scaling relation between \*CO on-top and O\* on-top adsorption energies; NEB pathways going through \*CO-top and O\*-bridge TS, and \*CO-top and O\*-top TS; BEP relations between  $E_{TS}$  with \*CO-top and O\*-bridge and descriptors utilizing O\*-top, O\*-bridge and O\*-hollow adsorption energies; parity plot between the predicted  $E_{TS}$  and the calculated ones; linear scaling relation between \*COOH on-top and \*CO on-top adsorption energies; BEP relations between the two kinds of  $E_{TS}$  and the \*COOH on-top adsorption energy plus half of the average adsorption energy for O\* at two neighboring top sites; NEB pathways for ternary alloys.

## References

- (1) Zhang, L.; Lin, C.-Y.; Zhang, D.; Gong, L.; Zhu, Y.; Zhao, Z.; Xu, Q.; Li, H.; Xia, Z. Guiding Principles for Designing Highly Efficient Metal-Free Carbon Catalysts. *Adv. Mater.* **2019**, *31*, 1805252.
- (2) Nørskov, J. K.; Bligaard, T.; Rossmeisl, J.; Christensen, C. H. Towards the Computational Design of Solid Catalysts. *Nat. Chem.* **2009**, *1*, 37–46.
- (3) Craig, M. J.; Coulter, G.; Dolan, E.; Soriano-López, J.; Mates-Torres, E.; Schmitt, W.; García-Melchor, M. Universal Scaling Relations for the Rational Design of Molecular Water Oxidation Catalysts with Near-zero Overpotential. *Nat. Commun.* **2019**, *10*, 1–9.
- (4) Andersen, M.; Levchenko, S. V.; Scheffler, M.; Reuter, K. Beyond Scaling Relations for the Description of Catalytic Materials. *ACS Catal.* **2019**, *9*, 2752–2759.
- (5) Yoo, J. S.; Schumann, J.; Studt, F.; Abild-Pedersen, F.; Nørskov, J. K. Theoretical Investigation of Methane Oxidation on Pd(111) and Other Metallic Surfaces. *J. Phys. Chem. C* **2018**, *122*, 16023–16032.
- (6) Ferrin, P.; Simonetti, D.; Kandoi, S.; Kunkes, E.; Dumesic, J. A.; Nørskov, J. K.; Mavrikakis, M. Modeling Ethanol Decomposition on Transition Metals: A Combined Application of Scaling and Brønsted-Evans-Polanyi Relations. *J. Am. Chem. Soc.* **2009**, *131*, 5809–5815.
- (7) Jacobsen, C. J.; Dahl, S.; Clausen, B. S.; Bahn, S.; Logadottir, A.; Nørskov, J. K. Catalyst Design by Interpolation in the Periodic Table: Bimetallic Ammonia Synthesis Catalysts. *J. Am. Chem. Soc.* **2001**, *123*, 8404–8405.
- (8) Singh, A. R.; Montoya, J. H.; Rohr, B. A.; Tsai, C.; Vojvodic, A.; Nørskov, J. K.



- Computational Design of Active Site Structures with Improved Transition-state Scaling for Ammonia Synthesis. *ACS Catal.* **2018**, *8*, 4017–4024.
- (9) Pallassana, V.; Neurock, M. Electronic Factors Governing Ethylene Hydrogenation and Dehydrogenation Activity of Pseudomorphic PdML/Re (0001), PdML/Ru (0001), Pd (111), and PdML/Au (111) Surfaces. *J. Catal.* **2000**, *191*, 301–317.
- (10) Logadottir, A.; Rod, T. H.; Nørskov, J. K.; Hammer, B.; Dahl, S.; Jacobsen, C. The Brønsted–Evans–Polanyi Relation and the Volcano Plot for Ammonia Synthesis over Transition Metal Catalysts. *J. Catal.* **2001**, *197*, 229–231.
- (11) Ding, Y.; Xu, Y.; Song, Y.; Guo, C.; Hu, P. Quantitative Studies of the Coverage Effects on Microkinetic Simulations for NO Oxidation on Pt (111). *J. Phys. Chem. C* **2019**, *123*, 27594–27602.
- (12) Wu, C.; Schmidt, D.; Wolverton, C.; Schneider, W. Accurate Coverage-dependence Incorporated into First-principles Kinetic Models: Catalytic NO Oxidation on Pt (111). *J. Catal.* **2012**, *286*, 88–94.
- (13) Liu, Z.-P.; Hu, P. General Trends in CO Dissociation on Transition Metal Surfaces. *J. Chem. Phys.* **2001**, *114*, 8244–8247.
- (14) Kropp, T.; Mavrikakis, M. Brønsted–Evans–Polanyi Relation for CO Oxidation on Metal Oxides Following the Mars–van Krevelen Mechanism. *J. Catal.* **2019**, *377*, 577–581.
- (15) Baz, A.; Holewinski, A. Understanding the Interplay of Bifunctional and Electronic Effects: Microkinetic Modeling of the CO Electro-oxidation Reaction. *J. Catal.* **2020**, *384*, 1–13.
- (16) Luo, L.; Nian, Y.; Wang, S.; Dong, Z.; He, Y.; Han, Y.; Wang, C. Real-Time Atomic-

- Scale Visualization of Reversible Copper Surface Activation during the CO Oxidation Reaction. *Angew. Chem., Int. Ed.* **2020**, *132*, 2526–2530.
- (17) Ambrosi, A.; Denmark, S. E. Harnessing the Power of the Water-Gas Shift Reaction for Organic Synthesis. *Angew. Chem., Int. Ed.* **2016**, *55*, 12164–12189.
- (18) Vogel, D.; Spiel, C.; Suchorski, Y.; Trincherro, A.; Schlögl, R.; Grönbeck, H.; Rupprechter, G. Local Catalytic Ignition during CO Oxidation on Low-Index Pt and Pd Surfaces: A Combined PEEM, MS, and DFT Study. *Angew. Chem., Int. Ed.* **2012**, *51*, 10041–10044.
- (19) Zhang, J.; Jin, H.; Sullivan, M. B.; Lim, F. C. H.; Wu, P. Study of Pd–Au Bimetallic Catalysts for CO Oxidation Reaction by DFT Calculations. *Phys. Chem. Chem. Phys.* **2009**, *11*, 1441–1446.
- (20) Xu, J.; White, T.; Li, P.; He, C.; Yu, J.; Yuan, W.; Han, Y.-F. Biphasic Pd-Au Alloy Catalyst for Low-temperature CO Oxidation. *J. Am. Chem. Soc.* **2010**, *132*, 10398–10406.
- (21) Liu, P.; Nørskov, J. K. Kinetics of the Anode Processes in PEM Fuel Cells—the Promoting Effect of Ru in PtRu anodes. *Fuel Cells* **2001**, *1*, 192–201.
- (22) Koper, M.; Lebedeva, N.; Hermse, C. Dynamics of CO at the Solid/liquid Interface Studied by Modeling and Simulation of CO Electro-oxidation on Pt and PtRu Electrodes. *Faraday Discuss.* **2002**, *121*, 301–311.
- (23) Song, C.; Tayal, A.; Seo, O.; Kim, J.; Chen, Y.; Hiroi, S.; Kumara, L.; Kusada, K.; Kobayashi, H.; Kitagawa, H., et al. Correlation Between the Electronic/local Structure and CO-oxidation Activity of Pd<sub>x</sub>Ru<sub>1-x</sub> Alloy Nanoparticles. *Nanoscale Adv.* **2019**, *1*, 546–553.

- (24) Zulkifli, N. D. B.; Ishimoto, T.; Sato, K.; Eboshi, T.; Nagaoka, K.; Koyama, M. Combined Theoretical and Experimental Studies of CO Oxidation on PdRu Nanoalloys. *Appl. Catal., A* **2018**, *568*, 176–182.
- (25) Dupont, C.; Jugnet, Y.; Loffreda, D. Theoretical Evidence of PtSn Alloy Efficiency for CO Oxidation. *J. Am. Chem. Soc.* **2006**, *128*, 9129–9136.
- (26) Liu, J.; Lucci, F. R.; Yang, M.; Lee, S.; Marcinkowski, M. D.; Therrien, A. J.; Williams, C. T.; Sykes, E. C. H.; Flytzani-Stephanopoulos, M. Tackling CO Poisoning with Single-atom Alloy Catalysts. *J. Am. Chem. Soc.* **2016**, *138*, 6396–6399.
- (27) Suntivich, J.; Xu, Z.; Carlton, C. E.; Kim, J.; Han, B.; Lee, S. W.; Bonnet, N.; Marzari, N.; Allard, L. F.; Gasteiger, H. A., et al. Surface Composition Tuning of Au–Pt Bimetallic Nanoparticles for Enhanced Carbon Monoxide and Methanol Electro-oxidation. *J. Am. Chem. Soc.* **2013**, *135*, 7985–7991.
- (28) An, K.; Alayoglu, S.; Musselwhite, N.; Plamthottam, S.; Melaet, G.; Lindeman, A. E.; Somorjai, G. A. Enhanced CO Oxidation Rates at the Interface of Mesoporous Oxides and Pt Nanoparticles. *J. Am. Chem. Soc.* **2013**, *135*, 16689–16696.
- (29) Falsig, H.; Hvolbæk, B.; Kristensen, I. S.; Jiang, T.; Bligaard, T.; Christensen, C. H.; Nørskov, J. K. Trends in the Catalytic CO Oxidation Activity of Nanoparticles. *Angew. Chem., Int. Ed.* **2008**, *120*, 4913–4917.
- (30) Pedersen, J. K.; Batchelor, T. A.; Yan, D.; Skjægstad, L. E. J.; Rossmeisl, J. Surface Electro-Catalysis on High-Entropy Alloys. *Curr. Opin. Electrochem.* **2020**, 100651.
- (31) Ferrari, A.; Dutta, B.; Gubaev, K.; Ikeda, Y.; Körmann, F. Frontiers in Atomistic Simulations of High Entropy Alloys. *J. Appl. Phys.* **2020**, *128*, 150901.
- (32) Raabe, D.; Ritchie, R. O.; George, E. High-Entropy Alloys. *Nat. Rev. Mater.* **2019**, *4*, 515–534.

- (33) Pickering, E.; Jones, N. G. High-entropy Alloys: A Critical Assessment of Their Founding Principles and Future Prospects. *Int. Mater. Rev.* **2016**, *61*, 183–202.
- (34) Batchelor, T. A.; Pedersen, J. K.; Winther, S. H.; Castelli, I. E.; Jacobsen, K. W.; Rossmeisl, J. High-entropy Alloys as a Discovery Platform for Electrocatalysis. *Joule* **2019**, *3*, 834–845.
- (35) Christoffersen, E.; Liu, P.; Ruban, A.; Skriver, H. L.; Nørskov, J. K. Anode Materials for Low-temperature Fuel Cells: A Density Functional Theory Study. *J. Catal.* **2001**, *199*, 123–131.
- (36) Stephens, I. E.; Bondarenko, A. S.; Perez-Alonso, F. J.; Calle-Vallejo, F.; Bech, L.; Johansson, T. P.; Jepsen, A. K.; Frydendal, R.; Knudsen, B. P.; Rossmeisl, J., et al. Tuning the Activity of Pt(111) for Oxygen Electoreduction by Subsurface Alloying. *J. Am. Chem. Soc.* **2011**, *133*, 5485–5491.
- (37) Bandarenka, A. S.; Varela, A. S.; Karamad, M.; Calle-Vallejo, F.; Bech, L.; Perez-Alonso, F. J.; Rossmeisl, J.; Stephens, I. E.; Chorkendorff, I. Design of an Active Site towards Optimal Electrocatalysis: Overlayers, Surface Alloys and Near-Surface Alloys of Cu/Pt(111). *Angew. Chem., Int. Ed.* **2012**, *124*, 12015–12018.
- (38) Mortensen, J. J.; Hansen, L. B.; Jacobsen, K. W. Real-space Grid Implementation of the Projector Augmented Wave Method. *Phys. Rev. B* **2005**, *71*, 035109.
- (39) Larsen, A. H.; Mortensen, J. J.; Blomqvist, J.; Castelli, I. E.; Christensen, R.; Duak, M.; Friis, J.; Groves, M. N.; Hammer, B.; Hargus, C., et al. The Atomic Simulation Environment—a Python Library for Working with Atoms. *J. Phys. Condens. Matter* **2017**, *29*, 273002.
- (40) Hammer, B.; Hansen, L. B.; Nørskov, J. K. Improved Adsorption Energetics within Density-functional Theory Using Revised Perdew-Burke-Ernzerhof Functionals. *Phys. Rev. B* **1999**, *59*, 7413.

- (41) Henkelman, G.; Uberuaga, B. P.; Jónsson, H. A Climbing Image Nudged Elastic Band Method for Finding Saddle Points and Minimum Energy Paths. *J. Chem. Phys.* **2000**, *113*, 9901–9904.
- (42) Gong, X.-Q.; Liu, Z.-P.; Raval, R.; Hu, P. A Systematic Study of CO Oxidation on Metals and Metal Oxides: Density Functional Theory Calculations. *J. Am. Chem. Soc.* **2004**, *126*, 8–9.
- (43) NIST-JANAF Thermochemical Tables. <https://janaf.nist.gov/>, Accessed: 2021-04-20.
- (44) Gajdo, M.; Eichler, A.; Hafner, J. CO adsorption on close-packed transition and noble metal surfaces: trends from ab initio calculations. *J. Phys. Condens. Matter* **2004**, *16*, 1141–1164.
- (45) Nilekar, A. U.; Greeley, J.; Mavrikakis, M. A Simple Rule of Thumb for Diffusion on Transition-Metal Surfaces. *Angew. Chem., Int. Ed.* **2006**, *45*, 7046–7049.
- (46) Baxter, R.; Hu, P. Insight into why the Langmuir–Hinshelwood Mechanism is Generally Preferred. *J. Chem. Phys.* **2002**, *116*, 4379–4381.
- (47) Öström, H. et al. Probing the transition state region in catalytic CO oxidation on Ru. *Science* **2015**, *347*, 978–982.
- (48) Xu, H.; Xu, C.-Q.; Cheng, D.; Li, J. Identification of Activity Trends for CO Oxidation on Supported Transition-metal Single-atom Catalysts. *Catal. Sci. Technol.* **2017**, *7*, 5860–5871.
- (49) Zhang, C.; Baxter, R.; Hu, P.; Alavi, A.; Lee, M.-H. A Density Functional Theory Study of Carbon Monoxide Oxidation on the Cu<sub>3</sub>Pt(111) Alloy Surface: Comparison with the Reactions on Pt(111) and Cu(111). *J. Chem. Phys.* **2001**, *115*, 5272–5277.

- (50) Sakong, S.; Groß, A. Methanol Oxidation on Pt(111) from First-Principles in Heterogeneous and Electrocatalysis. *Electrocatalysis* **2017**, *8*, 577–586.
- (51) Mehmood, F.; Rankin, R. B.; Greeley, J.; Curtiss, L. A. Trends in Methanol Decomposition on Transition metal Alloy Clusters from Scaling and Brønsted-Evans-Polanyi Relationships. *Phys. Chem. Chem. Phys.* **2012**, *14*, 8644–8652.
- (52) Clausen, C. M.; Batchelor, T.; Pedersen, J. K.; Rossmeisl, J. What Atomic Positions Determines Reactivity of a Surface? Longrange, Directional Ligand Effects in Metallic Alloys. *Adv. Sci.* **2021**, *8*, 2003357.
- (53) Wang, Z.; Hu, P. Rational Catalyst Design for CO Oxidation: A Gradient-based Optimization Strategy. *Catal. Sci. Technol.* **2021**, *11*, 2604–2615.
- (54) Kusada, K.; Kobayashi, H.; Ikeda, R.; Kubota, Y.; Takata, M.; Toh, S.; Yamamoto, T.; Matsumura, S.; Sumi, N.; Sato, K., et al. Solid Solution Alloy Nanoparticles of Immiscible Pd and Ru Elements Neighboring on Rh: Changeover of the Thermodynamic Behavior for Hydrogen Storage and Enhanced CO-oxidizing Ability. *J. Am. Chem. Soc.* **2014**, *136*, 1864–1871.

## TOC Graphic

